ALTERED STRUCTURE OF THE MN_4CA CLUSTER IN THE OXYGEN EVOLVING COMPLEX OF PHOTOSYSTEM II BY A HISTIDINE LIGAND MUTATION*

Junko Yano[1*], Lee M. Walker[2], Melodie A. Strickler[2], Rachel J. Service[2], Vittal K. Yachandra[1], and Richard J. Debus[2*]

From [1]Physical Biosciences Division, Lawrence Berkeley National Laboratory, Berkeley, CA 94720, USA, [2]Department of Biochemistry, University of California, Riverside, CA, 92521, USA

Running head: Altered Mn_4Ca cluster in a PSII mutant

Address correspondence to: Junko Yano, Physical Biosciences Division, Lawrence Berkeley National Laboratory, MS 66-0200, 1 Cyclotron Rd., Berkeley, CA 94720-8099, USA, E-mail: JYano@lbl.gov
Richard J. Debus, Department of Biochemistry, University of California, 3401 Watkins Drive, Riverside, CA, 92521-0129, USA, E-mail: richard.debus@ucr.edu

The effect of replacing a histidine ligand on the properties of the oxygen-evolving complex (OEC) and the structure of the Mn_4Ca cluster in Photosystem II (PSII) is studied by X-ray absorption spectroscopy using PSII core complexes from the *Synechocystis sp*. PCC 6803 D1 polypeptide mutant H332E. In the X-ray crystallographic structures of PSII, D1-His332 has been assigned as a direct ligand of a Mn ion, and the mutation of this histidine ligand to glutamate has been reported to prevent the advancement of the OEC beyond the $S_2Yz^{\bullet}$ intermediate state. The Mn K-edge absorption spectrum of D1-H332E shifts to a lower energy compared to that of the native wild type (WT) samples, suggesting that the electronic structure of the Mn cluster is affected by the presence of the additional negative charge on the OEC of the mutant. The EXAFS (Extended X-ray Absorption Spectrum) shows that the geometric structure of the cluster is altered substantially from that of the native WT state, resulting in an elongation of Mn-ligand and Mn-Mn interactions in the mutant. The Sr-H332E mutant, in which Ca is substituted by Sr, confirms that Sr(Ca) is a part of the altered cluster. The structural perturbations caused by the D1-H332E mutation are much larger than those produced by any biochemical treatment or mutation examined previously with X-ray absorption spectroscopy. The substantial structural changes provide an explanation not only for the altered properties of the D1-H332E mutant, but also the importance of the histidine ligand for proper assembly of the Mn_4Ca cluster.

The oxygen-evolving complex (OEC) located in the Photosystem II (PSII) membrane-bound protein in plant, algae, and cyanobacteria catalyzes the water-oxidation reaction (1-6). The OEC couples the four-electron chemistry of water oxidation with the one-electron photochemistry of the reaction center by sequentially storing oxidizing equivalents through five intermediate S-states (S_i, i = 0 to 4), before one molecule of dioxygen is evolved. The heart of the OEC consists of four Mn atoms and one Ca atom; the Mn_4Ca cluster provides a high degree of redox and chemical flexibility so that several oxidizing equivalents can be stored during the S-state cycle. Unlike inorganic catalysts, however, the uniqueness of catalytic centers in metalloenzymes arises from their protein environment. This environment provides (i) direct ligands to the cluster for maintaining the metal structure, while giving structural flexibility to the cluster at the same time, (ii) controls the cluster's redox potential by participating in charge distribution during the catalytic reaction, and (iii) provides a hydrogen-bonding network. Thus, nature has taken advantage of the special properties of the metal ions and tuned them by protein encapsulation to perform a wide variety of specific functions associated with life processes.

The assignment of the protein ligands to the Mn_4Ca cluster has been attempted by a wide range of mutational studies. These studies have revealed the potential ligands to the Mn_4Ca cluster. Considerable structural information has also been obtained through extensive studies by X-ray crystallography and various spectroscopic techniques over the past several years (1-5,7). The X-ray crystallography (XRD) studies up to the current resolution of 2.9 Å (8-11) have located the electron density associated with the water-oxidizing Mn_4Ca cluster within the large complex of PS II peptides. Structural ambiguity remains,

however, because of the limited resolution and radiation damage specifically to the Mn_4Ca cluster (12,13). The ligand environment of the Mn_4Ca cluster in the 3.5 and 3.0 (2.9) Å structural models also differ in a number of aspects, including the binding mode of the carboxylate ligands (i.e., bidentate versus monodentate) and the orientations of the backbone residues. These differences are likely due to the limited resolution of the diffraction data, different extents of radiation damage, and different interpretations of the electron density. Polarized X-ray spectroscopy with PSII single crystals also provides Mn_4Ca models based on the accurate distances and the polarization characteristics of metal-metal or metal-ligand vectors within the protein environment (14). However, the assignment of the ligand environment remains tentative in this case because the proposed OEC environment obtained by this method is a simple combination of the Mn_4Ca cluster model obtained from the polarized EXAFS and the ligand environment from the crystal structure (Fig. 1).

Despite the structural ambiguities mentioned above, all the experimental evidence so far points that His332 residue is an important direct ligand to the Mn_4Ca cluster. In the recent X-ray crystallographic structural models of PSII, the Mn_4Ca cluster is ligated by a single histidine residue, His332 of the D1 polypeptide (8-11). This assignment is supported by recent 31 – 34 GHz ESEEM studies of the Mn_4Ca cluster in its S_2 state (15,16). These studies show that the nitrogen couplings observed in earlier ESEEM studies conducted at lower frequencies (9 – 12 GHz) (17-20) originate from a single ^{14}N nucleus. The higher frequency studies permit the quantitative determination of the hyperfine and nuclear quadrupolar couplings of the coupled nucleus; these are consistent with direct coordination of the ^{14}N atom to a Mn ion in the S_2 state (15,16). On the basis of earlier 9 GHz ESEEM studies conducted with unlabeled and [^{15}N]histidine, this ^{14}N atom is known to originate from the _ nitrogen of a histidine imidazole group (19,21). Because the ^{14}N coupling essentially disappears in PSII core complexes from the D1-H332E mutant of *Synechocystis* sp. PCC 6803 (20), the ^{14}N nucleus has long been assigned to D1-His332, consistent with the X-ray structural models (e.g., (5)).

However, in a recent study (22) of a different mutant, D1-H332S, of *Synechococcus elongatus* the nitrogen coupling observed in the three-pulse 9 GHz ESEEM spectrum of wild-type PSII core complexes was largely unchanged by the D1-H332S mutation. It was proposed that the nitrogen coupling observed in all the ESEEM studies originates from D1-His337 rather than D1-His332 and that the loss of the nitrogen coupling in the D1-H332E mutant (20) was caused by secondary structural perturbations introduced into PSII by the mutation. These same structural perturbations were proposed (22) to give rise to the altered S_2 state multiline EPR signal that is observed in the D1-H332E mutant (20,23) and the inability of D1-H332E cells (24) and PSII core complexes (23) to advance beyond the $S_2Y_Z^{\bullet}$ state.

To study whether the failure of the catalytic cycle of D1-H332E is due to the structural changes of the OEC itself, or to the secondary effect of the mutation, we applied X-ray spectroscopy in the current study. Manganese X-ray absorption spectroscopy is exquisitely sensitive to changes in Mn-Mn and Mn-Ca vectors in the Mn_4Ca cluster of PSII and to changes in the charge density on the Mn ions. Moreover, XAS can detect the signals from Mn or Ca/Sr even when there are no other spectroscopic signatures from the cluster, as the X-ray spectroscopic signals are never silent. This property is useful in studying whether the cluster assembles in the mutant species. For example, it is possible that the cluster assembles in a modified geometry which makes it inactive and or incapable of exhibiting other spectroscopic signals. Determining the geometric and electronic structure of such altered clusters in mutants is particularly important because the changes may give us a rationale for identifying the properties of the native cluster that make it unique for catalyzing the difficult water oxidation reaction. XAS is also useful for studying the changes in the geometric and electronic structures as the altered cluster advances through the S-state cycle, and in determining the state at which the cycle is impaired. These structure-function correlations in the altered structures that may assemble in some mutants can be critical for understanding the native, active catalytic cluster. Accordingly, to characterize structural perturbations that may be caused by the D1-H332E mutation and to further investigate the structural role of D1-His332 in the

Mn_4Ca cluster of PSII, we conducted a Mn X-ray absorption study of the D1-H332E mutant of *Synechocystis* sp. PCC 6803.

Experimental Procedures

Construction of Mutant and Propagation of Cultures. The construction of the D1-H332E mutation was described previously (20). Briefly, the mutation was introduced into the *psbA-2* gene of *Synechocystis* sp. PCC 6803 and transformed into a host strain of *Synechocystis* that lacks all three *psbA* genes and that contains a hexahistidine-tag (His-tag) fused to the C-terminus of CP47. Solid media contained 5 mM glucose, 10 μM DCMU, and 5 _g/mL kanamycin monosulfate. The DCMU and antibiotic were omitted from the liquid cultures. Large-scale liquid cultures (each consisting of three 7 L cultures held in glass carboys) were propagated as described previously (25). For the isolation of Sr-containing PSII core complexes, the $CaCl_2$ in the liquid media was replaced with an equivalent concentration of $SrCl_2$ (26,27). To verify the integrity of the mutant cultures that were harvested for the purification of PSII core complexes, an aliquot of each culture was set aside and the sequence of the relevant portion of the *psbA-2* gene was obtained after PCR amplification of genomic DNA (28).

Purification of PSII core complexes. PSII core complexes of the wild type (WT) and D1-H332E mutant of *Synechocystis* sp. PCC 6803 retaining the Mn cluster were purified under dim green light at 4 °C with Ni-NTA superflow affinity resin (Qiagen, Valencia, CA) as described previously (27). The purification buffer consisted of 1.2 M betaine, 10% (v/v) glycerol, 50 mM MES-NaOH (pH 6.0), 20 mM $CaCl_2$, 5 mM $MgCl_2$, 50 mM histidine, 1 mM EDTA, and 0.03% (w/v) *n*-dodecyl _-D-maltoside. To ensure that Sr-containing PSII core complexes contained no excess Sr ions, Sr-containing PSII was purified in the presence of buffers containing $CaCl_2$. The purified PSII core complexes were concentrated to ~ 1.0 mg of Chl/mL by ultrafiltration, and stored in liquid N_2.

Preparation of Samples for X-ray Absorption Studies. To prepare samples for the X-ray absorption studies, the PSII core complexes were transferred to a buffer containing 1.2 M betaine, 40% (v/v) glycerol, 50 mM MES-NaOH (pH 6.0), 20 mM $CaCl_2$, 5 mM $MgCl_2$, and 0.03% (w/v) *n*-dodecyl _-D-maltoside by concentrating them to ~ 9 mg of Chl/mL, diluting them 20-fold with a buffer containing 42% (v/v) glycerol, then again concentrating them to ~ 9 mg of Chl/mL. The resulting concentrated PSII core complexes were transferred to epoxy sample holders (40 μl each) designed to fit into both EPR and X-ray liquid He cryostats. After dark-adaptation for one hour at room temperature, the samples were predominantly in the S_1 state. These samples were stored in liquid nitrogen until used. Half of the S_1 sample holders were taken out later and illuminated with a 400 W tungsten lamp at 200 K for 5 minutes in order to generate the S_2 state for the wild type S_2 state and at 273 K for 2 minutes for the H332E mutant sample. The illuminated samples were then stored in liquid nitrogen.

EPR measurements. Samples were characterized by EPR spectroscopy at 8 K in order to ensure the quality of the samples before and after the illumination. Spectra were collected using a Varian E-109 EPR spectrometer equipped with an Air Products Helitran liquid helium cryostat. The generation of the S_2 state after the illumination was checked by the intensity of EPR multiline signal characteristic to the S_2 state. All the samples were also checked with EPR prior to XAS measurement to see whether free Mn(II) was produced during any biochemical and sample handling processes. No detectable Mn(II) signal was observed for any of the mutant and wild type samples.

XAS measurements. X-ray absorption spectroscopy (XAS) was performed at the Stanford Synchrotron Radiation Laboratory (SSRL) on beamline 9-3 at an electron energy of 3.0 GeV with an average current of 85-100 mA. The radiation was monochromatized by a Si(220) double-crystal monochromator. The intensity of the incident X-ray beam was monitored by a N_2-filled ion chamber (I_0) in front of the sample. The monochromator energy was calibrated using a pre-edge peak of $KMnO_4$ (6543.3 eV) for Mn XAS, and using an edge peak of strontium acetate (16120 eV) for Sr XAS. These standards were placed between two N_2-filled ionization chambers (I_1 and I_2) after the sample. The total number of X-ray photons used for the measurements was ~ 4 x 10^{13} photons mm^{-2} for the Sr XAS (16-17 keV) and ~ 5 x 10^{12} photons mm^{-2} for the Mn XAS (6-7

keV), and are well below the X-ray damage threshold as previously established (12). The Mn K-edge was also closely monitored for any reduction of Mn as seen by a shift in the K-edge inflection point energy. The monochromator was detuned at 6600 eV (16200 eV for Sr) to 50% (or greater) of maximal flux to attenuate the X-ray 2nd harmonic. Samples were kept at 10 K in a liquid helium flow cryostat to minimize radiation damage. Data reduction of the XAFS spectra was performed using EXAFSPAK (29). Pre-edge and post-edge background were subtracted from the XAS spectra and the results were normalized with respect to edge height. After conversion of background-corrected spectra from energy space to photoelectron wave vector (k) space (E_0 = 6561.3 eV for Mn and 16120 eV for Sr), and weighted by k^3, a four-domain spline function was subtracted. Curve fitting was performed using ab initio calculated phases and amplitudes from the program FEFF 8.2. (30,31). The details of the curve fitting analysis is described in the supplementary information.

Results

Mn XANES of D1-H332E. The XAS spectra of *Synechocystis sp.* PCC 6803 wild type (WT) and D1-H332E PSII core complexes in the dark state (S_1) and illuminated (S_2) state are compared in Figure 2. The WT S_1 and S_2 XANES spectra are similar to those observed in spinach PSII membrane preparations (32), in which the formal oxidation states have been assigned as $Mn(III)_2Mn(IV)_2$ for the S_1 state and $Mn(III)Mn(IV)_3$ for the S_2 state. During the S_1 to S_2 transition, the rising edge energy shifts ~ 0.7 eV to higher energy in the WT (Fig. 2a). In its dark state (S_1), the D1-H332E mutant has a lower rising edge energy and a slightly different shape as seen in the second derivatives than the WT S_1 state (Fig. 2b). This is not due to the release of free Mn(II) in the mutant samples as no Mn(II) signal was observed in the EPR spectra taken prior to the XAS measurement. One possible explanation for this low energy shift in D1-H332E is that the formal oxidation state of the D1-H332E dark state is not $Mn(III)_2(IV)_2$, but lower such as $(III)_3(IV)$ or $(II)(III)(IV)_2$. The energy shift between the WT and the D1-H332E is 1.69 eV. This is much larger than the energy shift between the S_1 to S_2 transition of the WT, but within the range of one-oxidation state differences (for example, shifts of ~2.1 eV for the S_0 to S_1 transition and ~1.1 eV for the S_1 to S_2 transition have been observed in spinach PSII membrane preparations (32)). This variation in the magnitude of the energy shift corresponding to a single oxidation event demonstrates the difficulties of making formal oxidation state assignments on the basis of the XANES edge shift: the edge shape is also highly sensitive to structural changes.

In H332E PSII core complexes, only ~ 60% of the PSII centers contain Mn clusters, although all of these advance to the S_2 state in response to continuous illumination at 273 K (23). Upon illumination at 273K, the H332E XANES spectrum shifts ~0.6 eV towards higher energy (Fig. 2(c)), indicating that Mn is oxidized during this transition in the mutant similar to the WT. The dark state of D1-H332E is EPR silent, and upon illumination, exhibits an altered multiline EPR spectrum that superficially resembles that in Ca-depleted, Sr-substituted, and NH_3-inhibited WT PSII preparations (20,23). It is therefore likely that the formal oxidation state of the D1-H332E mutant in its dark state is the same as that of the WT, i.e. $Mn(III)_2Mn(IV)_2$.

Mn EXAFS of D1-H332E. Figure 3 shows the Fourier transforms of k^3-weighted Mn EXAFS spectra of *Synechocystis sp.* PCC 6803 WT and D1-H332E PSII core complexes in the dark (S_1) and illuminated (S_2) states (k-space data shown in Figure S1 in Suppl. Info.). The WT spectra (Fig. 3a) are almost identical to those of the S_1 and S_2 spectra of spinach PSII membrane preparations, suggesting that the structure of the Mn_4Ca cluster in the S_1 and S_2 states is the same in *Synechocystis* as in spinach. The D1-H332E mutant dark (S_1) state spectrum (Fig. 3b) differs significantly from that of the WT S_1 state spectrum (Fig. 3a). The first FT peak (labeled I in Figs. 3a and 3b), which arises primarily from Mn-O interactions with a possible small contribution from one or two Mn-N interaction(s) in the WT, becomes more intense and shifted towards longer distance in the mutant. In addition, the second FT peak (labeled II in Figs. 3a and 3b), which largely arises from the di-μ-oxo bridged Mn-Mn interactions in the WT, decreases and merges with the third peak (labeled III in Fig. 3a and 3b, and assigned predominantly to oxo-

bridged Mn-Mn and Mn-Ca distances at ~ 3.3 and ~ 3.4 Å in the WT) in the mutant. These changes indicate that the D1-H332E mutation substantially alters the structure of the Mn_4Ca cluster. The spectra obtained with three different preparations of D1-H332E PSII core complexes were identical. This reproducibility provides proof that the structure of the OEC cluster in the mutant is homogeneous, and that it does not change as a function of the preparation. Additionally, we estimated that the Mn stoichiometry in the D1-H332E mutant is the same as the native PSII, *i.e.*, 4 Mn ions per PSII, based on previous EPR studies (20, 23) and the analysis of Mn X-ray fluorescence data (see Suppl. Info.).

Upon illumination, the first FT peak intensity decreases in the mutant (Fig. 3b, gray trace). Because the first FT peak of the WT is essentially unchanged upon illumination (Fig. 3a, gray trace), the substantially decreased amplitude of the first FT peak in the mutant indicates that substantial structural changes (e.g., ligand reorganization) take place during the S_1 to S_2 transition in the mutant, whereas little or no structural change takes place during this transition in WT (33).

Sr XAS on Sr-substituted H332E. It has been suggested on the basis of biochemical studies that mutations of D1-His332 diminish the affinity of Ca for the Mn_4Ca cluster (34). Because the X-ray crystallographic structural models place the Ca ion and His332 ligand on opposite sides of the Mn_4Ca cluster, the apparently diminished affinity of Ca has been hypothesized to be a consequence of mutation-induced perturbations to the Mn_4Ca cluster. In order to investigate whether the Ca ion is present in the Mn cluster of D1-H332E PSII core complexes, samples were prepared having Sr substituted for Ca and measurements were carried out using Sr XAS (instead of Ca XAS). Many studies have shown that the Ca ion can be replaced with Sr while retaining O_2-evolving activity in PSII (26,27,35). Additionally, Sr XAS (absorption energy: ~16120 eV) has several experimental advantages over Ca XAS (absorption energy: ~ 4500 eV), such as (i) the X-ray radiation damage is less for the same number of photons incident on the sample, (ii) the attenuation of the incident and scattered X-rays is far less at the Sr X-ray absorption energy, and (iii) the fluorescence yield of Sr is higher than that of Ca (see references (36,37)).

Figure 4 shows the Sr XANES (a) and EXAFS (b) spectra of Sr-substituted H332E PSII core complexes. For a comparison, the published data of the Sr-WT PSII core complexes from *Synechococcus elongatus* in the S_1 state is shown in the figure. The Sr EXAFS of the mutant (Fig. 4b, gray trace) shows a distinctive second FT peak (arising primarily from Mn-Sr interactions) that closely resembles the second FT peak in the WT. These data show that the Mn-Sr interaction exists in the H332E mutant and that the Mn-Sr interaction(s) is(are) at a similar distance and amplitude to the WT. On the other hand, the first FT peak in the mutant (corresponding to Sr-O interactions) is much stronger than in the WT. We also collected Mn XAS on this sample, in order to see if the substitution of Sr for Ca caused any structural perturbations to the Mn_4 cluster (Figure S2 in Suppl. Info.). Unlike the situation in *Synechococcus elongatus,* where biosynthetically incorporated Sr does not exchange with exogenous Ca ions (26), Sr/Ca exchange occurs when *Synechocystis* PSII core complexes containing biosynthetically incorporated Sr are purified in buffers containing Ca (27). Because Sr XAS requires the elimination of exogenous Sr ions, our PSII core complexes containing biosynthetically-incorporated Sr were purified in Ca-containing buffers. Therefore, only about 75% of the Sr-H332E PSII core complexes contained Sr, while the remainder contained Ca (27). This heterogeneity is not an issue for carrying out Sr XAS measurements, because only the Sr-H332E fraction is probed. For Mn XAS on this sample, on the other hand, both Sr-H332E and Ca-H332E fractions contribute to the spectrum, and we cannot distinguish their individual contributions (Fig. S2 in Suppl. Info.). In the Mn EXAFS shown in Fig. S2, the spectra of the Ca-H332E and Sr(Ca)-H332E PSII samples are almost identical up to the FT peak II region, but the FT peak III region differs significantly. This difference might be explained as a consequence of a larger contribution of the Sr H332E fraction which results in a distance elongation (typically, actual distance of 3.4 Å for Mn-Ca and 3.5 Å for Mn-Sr) and increase in the intensity (due to heavier atom contribution) around the peak III region. Although further detailed structural information cannot be extracted from the Mn XAS on the Sr-H332E sample, the geometry of the Mn_4 cluster in the Sr-

containing H332E sample seems to be very similar to that in the Ca-containing H332E sample.

Mn EXAFS Curve fitting of the WT S_1 state spectrum. Mn EXAFS curve fits were carried out for the k^3-weighted EXAFS spectra of the WT S_1 state and the D1-H332E mutant dark state (S_1). Fitting results for the WT S_1 state for the Mn-nearest neighbor interactions are given in Table 1, in which R, N, and σ^2 show actual distance (Å) (note the Fourier transforms only show apparent distances), coordination number, and EXAFS Debye-Waller factor (Å^2), respectively. N values are defined as the total number of absorber-backscatterer vectors divided by the number of absorber atoms per OEC. R factor (R_f, %) shows the goodness of the fit.

The predominant contribution to the FT peak I is from Mn-oxygens at R= ~ 1.87 Å. Although one or two Mn-nitrogen interaction(s) from the histidine residue(s) contributes to this region, it cannot be distinguished in the data because of the minor contribution (one out of ~24 Mn-ligand interactions at similar distances). Therefore, Mn-O and Mn-N interactions were treated together in the current curve fitting.

The second and third peak region (Fig. 3a) is due mainly to the di-μ-oxo bridged Mn-Mn (~ 2.7 Å), and mono-μ-oxo-bridged Mn-Mn (~3.3 Å) interactions. The presence of Mn-Ca interactions (3.4 Å) in addition to the predominant mono-μ-oxo bridged Mn-Mn interaction in the third peak has previously been demonstrated on the basis of Ca XAS experiments conducted with spinach PSII preparations (Sr XAS experiments on Sr-substituted PSII show four Mn-Sr interactions between ~3.5 and 4.0 Å, see below) (37). Therefore, Mn-Ca interactions are included in the fit. In Table 1, the most preferable structural motif that supports the vector components of the recent EXAFS studies (the ratio of di-μ-oxo bridged Mn-Mn : mono-μ-oxo bridged Mn-Mn : Mn-O-Ca bridged interactions = 3:1:x, x=2 or 3, Figure S3, A-D in Suppl. Info.) was used for fitting the WT S_1 state spectrum. The contribution of three Mn-Mn interactions and their distance heterogeneities (2.7 to 2.8 Å) becomes clear only when the polarized spectra or the range-extended EXAFS data are used for the fit (38,39). Therefore, this heterogeneity was not considered in this study. Including Mn•••C interactions, which arise from the second shell carbons at ~ 3.2 Å from Mn, slightly improves the fitting quality. Although the coordination number, N=2.75 for the Mn•••C interactions was used through the fits which is based on the ligand model reported in the 2.9 Å crystal structure (11), this number remains highly ambiguous due to the uncertainly in the ligand binding modes (for example, whether the binding modes of the carboxylate ligands are bidentate or monodentate). Nevertheless, the Debye-Waller factor (σ^2) of this absorber-backscatterer path is large (~ 0.018 Å^2), indicating that the distance distribution of the Mn•••C interactions is high, and its contribution to the EXAFS spectrum has only a minor effect. In addition, the inclusion of this path does not noticeably change the fitting parameters for the other paths.

We have also considered two shell contributions to the first FT peak region, one part from the Mn-bridging oxygen and the other from the Mn-terminal oxygen. We assumed that the Mn-bridging oxygens have shorter distances (~ 1.8 Å) than those of the Mn-terminal oxygens (1.9 Å) on the basis of model compound studies (40,41). No obvious improvement was observed in the two shell fit (not shown). The Fit#2 and 4 (Table 1) are shown in Figure 5a.

Mn EXAFS Curve fitting of the D1-H332E spectra. Table 2 summarizes the curve fitting results of the D1-H332E mutant in its dark-stable state (S_1). In Fig. 3b, the increased intensity and the longer distance shift of the first FT peak of the D1-H332E sample compared to that of the WT indicates that the Mn-ligand distances are more uniform in the mutant. The one shell fit of the first peak gives a Mn-ligand distance of 1.89 Å in the mutant while it is ~1.86 Å in the WT, suggesting that an elongation of the Mn-ligand interactions occurs in the mutant (see also Table S1 in Suppl. Info.).

The averaged Mn-Mn distance (peak II) is also longer (~2.77 Å) in the mutant compared to the WT (~2.72 Å). On the other hand, the intensity of the peak II region is decreased significantly in the mutant. This could be either due to the increased distance heterogeneity in the ~ 2.7 Å region, or due to the reduced number of di-μ-oxo bridged Mn-Mn interactions in the mutant. In order to test these two hypothesis, N of the Mn-Mn ~ 2.7 Å interaction was fixed either to N=1 (two Mn-Mn interactions,) or to N=1.5 (three Mn-Mn

interactions) in the fit (3:1:x and 2:1:x, or 3:2:x and 2:2:x). The result between two or three Mn-Mn2.7Å interactions was not conclusive as the fitting quality is similar within the error of the method (for example, Fit#1 compared to Fit#7 in Table 2). The result, however, shows that the averaged di-μ-oxo-bridged Mn-Mn distance is about 0.05 Å elongated in the mutant. If there are three di-μ-oxo bridged Mn-Mn interactions, the distance heterogeneity is much higher than that of the WT based on the decreased intensity of peak II.

The presence of the Mn-Ca(Sr) interactions was confirmed by the Sr XAS data obtained with the Sr-substituted H332E PSII core complexes, described below. Therefore, the Mn-Ca interaction was included in all the fits. The mono-μ-oxo bridged Mn-Mn interaction (~ 3.2 Å) seems to be necessary for maintaining a reasonable fit quality, and elimination of this interaction made fit quality worse (not shown). This implies that the unclear peak III region in the mutant spectrum (Fig. 3b) is a consequence of the elongation of peak II components.

Fits corresponding to an increase in the Mn-Mn 3.3 Å interactions to two as compared to one in the WT, namely 3:2:x and 3:1:x, or 2:2:x and 2:1:x, were also considered without much improvement in the quality of the fit. The addition of the second shell Mn•••C(ligand) ~ 3.1 Å interactions slightly improved the R factor. However, the contribution of this absorber-backscatterer path has only a minor impact on the modeling of the Mn_4Ca cluster due to its high Debye-Waller factor and it is not included in the Table. The representative fits (Fit# 2 and 8) are shown in Fig. 5b.

Sr EXAFS Curve fitting of the D1-H332E spectra. Fitting results for the Sr XAS on Sr-H332E are given in Table 3. Previously, Ca EXAFS of native PS II and Sr EXAFS of Sr-reactivated spinach PSII membranes showed the proximity of Ca to Mn at 3.4 Å, and Sr to Mn at 3.5 Å in the dark-stable S_1 state (36,42,43). A more recent study on Sr-substituted PSII core complexes from *Synechococcus elongatus* shows Sr to be proximate to all four of the Mn in the Mn_4 cluster in all S-states (37). The study shows that there are two to three Sr-Mn interactions in which Sr and Mn are likely to be bridged by μ-oxo groups around 3.5 Å, while there are two or one longer interactions around 3.9 Å. The fitting results of the published Sr-substituted PSII core complexes from *Synechococcus elongatus* is shown in Table S2 in the Suppl. Info.

FT peak I in Fig. 4(b) is best simulated by one shell of 7 to 8 oxygen atoms at R= 2.56 Å. For convenience, the N number of the Sr-O 2.5 Å interaction was fixed to 8 in Table 3. The Debye-Waller factor of this peak is much smaller (0.005) in the mutant than in the WT (Table S2). Assuming that the coordination number of Sr is the same in the WT and mutant samples, the result suggests that the Sr-O distance is more uniform in the mutant compared to the WT. On the other hand, FT peak II, which is best fit with two to three shorter Sr-Mn interactions and two to one longer Sr-Mn interaction (37) in the Sr-WT PSII core complexes, appeared with the same intensity in the two samples, suggesting that the Mn-Sr binding modes are similar between the WT and the mutant. Fit#1 and 2 are shown in Figure 6. The R_f value of Fit#1 is slightly better than others and preferable, suggesting that there are three short (~3.5 Å) and one long (~ 3.9 Å) Sr-Mn interactions similar to that seen in the WT.

Discussion

Structural changes of the OEC in the H332E mutant. The D1-H332E mutant of *Synechocystis* sp. PCC 6803 has previously been characterized with chlorophyll fluorescence (24,34) and thermoluminescence (24) measurements in intact cells, and with optical absorption (23), EPR (20,23) and ESEEM (20) measurements in PSII core complexes. These data show that, in the mutant, the temperature threshold for forming the S_2 state is approximately 100 K higher than in WT, that the quantum yield for forming the S_2 state is very low, corresponding to a dramatic slowing of electron transfer from the Mn cluster to $Y_Z^{\bullet}$, that the S_2/S_1 midpoint potential is substantially decreased, that Mn oxidation beyond the $S_2Y_Z^{\bullet}$ state is blocked, and that the S_2 state multiline EPR signal is altered, exhibiting more hyperfine lines and narrower splittings than in WT. In addition, D1-H332E PSII core complexes exhibit no S_1 state multiline EPR signal (23). These data were interpreted as showing that although the Mn cluster is assembled in the altered

ligand environment, the mutation perturbs the structure of the Mn_4Ca cluster and the network of hydrogen bonds that facilitates the S_2 to S_3 transition (20,23,24). Compared to the energy scale of EPR or IR spectroscopy, the energy scale of XAS is much larger (1 eV shift in the edge corresponds to 8066 cm^{-1}). Thus changes in XANES would indicate much larger changes in the electronic/geometric structure that would also be reflected in the substantial changes in the EXAFS. In the current study, the XAS data show that the D1-H332E mutation substantially alters the structure of the Mn_4Ca cluster in both the S_1 and S_2 states, resulting in an elongation of Mn-ligand and di-μ-oxo bridged Mn-Mn interactions in the mutant. These structural alterations are far greater than those caused by any mutation (unpublished data) or biochemical treatment examined previously by X-ray absorption spectroscopy, including Ca-depletion (44), Sr/Ca exchange (45), and NH_3-inhibition (46).

The lower rising edge energy, and the changes in the shape in the XANES spectrum of the D1-H332E PSII core complexes in its dark-stable (S_1) state could originate from a change in Mn oxidation state or from a change in charge density on the Mn cluster caused by a change in cluster structure, ligand symmetry, or ligand exchange. Because dark-adapted D1-H332E PSII core complexes (EPR silent) produces a multiline EPR signal upon illumination, which is evidence for a paramagnetically coupled 4Mn cluster, we conclude that the formal oxidation state of dark-adapted D1-H332E PSII centers is the same as that of the WT, i.e. $Mn(III)_2Mn(IV)_2$. Therefore, the XANES shift to lower energy compared to WT probably results from a combination of (1) increased negative charge density on Mn caused by, for example, replacing a neutral histidyl nitrogen with a negative carboxylate oxygen and (2) accompanying structural changes of the Mn_4Ca cluster.

The presence of a Ca (Sr) ion in the Mn cluster of D1-H332E is confirmed by the similar intensity of the Mn-Sr interactions observed in the Sr EXAFS of the mutant.

The Mn EXAFS curve fitting result suggests that the Mn_4Ca cluster in D1-H332E contains two to three di-μ-oxo bridged Mn-Mn units, one to two mono-μ-oxo bridged Mn-Mn unit, and two to three ~ 3.5 Å Mn-Ca interactions. In the one shell fit, the averaged distance of di-μ-oxo-bridged Mn-Mn interaction in the mutant is changed from ~2.72 Å (WT) to ~2.77 Å (Tables 1 and 2). A possible reason for this elongation is a protonation of the oxo-bridge (Figure 7a), presumably to restore the charge balance because of the replacement of a neutral histidine ligand by a negatively charged glutamate residue. Another is a ligand structural change, where the replacement of the histidine residue by a glutamate triggers a previously bridging bidendate carboxylate changing its coordination mode from bidentate to monodentate (Figure 7b). In the case of protonation of an oxo-bridge, we expect about a 0.1 Å elongation of the Mn-Mn distance (47). In the case of a carboxylate changing its coordination mode, removal of a bidentate-type bridge could elongate the di-μ-oxo bridged Mn-Mn distance also by 0.1 Å, such as is observed between the di-μ-oxo/μ-carboxylato and the di-μ-oxo species (48). The proposed scenarios for the distance elongation suggested above could also occur by replacing His332 by another proximal carboxylate residue or water molecule.

Regarding the structural motif of the altered Mn_4Ca cluster in the mutant, the following two possibilities are considered. If there are three di-μ-oxo-bridged Mn-Mn interactions, as in models having (3:1:x) or (3:2:x) configurations (shown in Fig. S3, Suppl. Info.), the distance heterogeneity would be greater in D1-H332E than in WT in addition to the Mn-Mn distance being elongated. In recent polarized XAS and range extended XAS studies, the presence of three di-μ-oxo-bridged Mn-Mn interactions having 2.7Å:2.8Å distances in a 2:1 ratio has been suggested (39,49). In the D1-H332E mutant, we would expect an elongation (to >2.8 Å) of the longer component and/or an increased fraction of the longer component: in either case, peak II will be shifted to a longer distance and the intensity will be decreased. If there are two di-μ-oxo-bridged Mn-Mn interactions as in the model having a (2:1:x) or (2:2:x) configurations in Fig. S3, Suppl. Info., one or both of the distance(s) would be elongated in the mutant.

Accompanied by the elongation and weak intensity of the ~ 2.7 Å Mn-Mn interaction (peak II), there is a strong Mn-ligand FT peak I in the D1-H332E dark state. This suggests a more

symmetric Mn-O ligand environment, which could happen if an oxo-bridge is broken, ligands are ligated as monodentate instead of bidentate, or water is ligated instead of carboxylate in the altered OEC (Figure 7b).

In the Sr XAS experiments, a stronger Sr-O FT peak was observed in D1-H332E than in the WT, just as a stronger Mn-ligand peak was observed in the Mn XAS of the mutant. This is likely due to a more uniform Sr-O environment and elongation of the Sr-O distances in the mutant. Although typical Sr-O(carboxylate) and Sr-O(water) distances are both within the range of 2.5 – 2.7 Å and therefore cannot be discriminated on the basis of the distance, a more symmetric Sr-O environment may occur, for example, when a carboxylate residue ligated to Sr is replaced with a water molecule. One possibility is that the mutation-induced alteration of the Mn_4 cluster structure causes the rearrangement of the ligands around the Sr(Ca), and that a water molecule ligates to the Mn_4 cluster in place of a carboxylate group. On the other hand, the Sr-Mn interactions are similar in the mutant and WT. On the basis of these observations, we consider the following two cases for the Mn-Sr(Ca) interactions: (i) the Mn-Sr(Ca) binding modes are the same in the WT and the mutant, but the hydrogen bonding network is changed; for example, more water molecules ligate to Sr(Ca) instead of carboxylate oxygen atom(s), or (ii) the Mn-Sr(Ca) binding mode is altered, but the number of the Mn-Sr(Ca) interactions remains the same.

D1-His332 is a Ligand of the Mn_4Ca cluster. As noted above, the structural perturbations caused by the D1-H332E mutation are substantially larger than those produced by any biochemical treatment or mutation examined previously with XAS, including the extraction of Ca from the Mn_4Ca cluster. Whereas Ca-depletion, Sr/Ca exchange, and NH_3-inhibition all alter the S_2 state multiline EPR signal in the same manner as the D1-H332E mutation, Mn-EXAFS studies show that these treatments alter the structure of the Mn_4Ca cluster either negligibly (in the case of Sr substitution) or to much lesser extents than the D1-H332E mutation (in the case of Ca extraction). Only in the case of NH_3-inhibition, where NH_3 is proposed to enter the coordination sphere of the Mn_4Ca cluster as a amido bridge between two Mn ions (50), was elongation of a Mn-Mn distance observed (from 2.72 Å to 2.87 Å) (46).

One significant difference of the mutation compared to the above treatments is that the Mn_4Ca cluster must necessarily be assembled in a different ligand environment in the mutant. In the WT, the D1 and CP43 protein subunits of PSII provide ligands to the OEC: the current view of the assembly process is that the first two Mn^{2+} ions are bound and photooxidized into Mn^{3+} during their assembly into the apoprotein and then the binding of the subsequent Mn^{2+} ions occurs (51,52). Whether the ligands that are required for the assembly are the same as the proposed direct ligands to the Mn_4Ca cluster remains a question. Nevertheless, the fact that the Mn_4Ca cluster can assemble in the His332Glu mutant but in an altered structure, suggests that a different ligand environment has modified the Mn_4Ca cluster. On the basis of the earlier Mn-EXAFS studies of Ca-depleted, Sr/Ca-exchanged, and NH_3-inhibited PSII preparations, it is difficult to imagine how the D1-H332E mutation could cause the substantial structural perturbations to the Mn_4Ca cluster observed in our Mn-EXAFS data if D1-His332 is not directly coordinated to a Mn ion. Therefore, we conclude that our data are in support of the X-ray crystallographic models depicting D1-His332 as a ligand to a Mn ion. Upon mutation of D1-His332 to glutamate, the missing imidazole ligand must be replaced by another ligand/residue, such as (i) a glutamate carboxylate, (ii) another carboxylate residue, (iii) a water molecule, or (iv) another histidine ligand. Another possibility is that, (v) no new residue is ligated to the Mn and the coordination number therefore changes from six to five. Alternatively a combination of those possibilities could occur if the reorganization of several ligands is triggered by the D1-H332E mutation. The Mn XANES spectrum of D1-H332E helps to distinguish between these possibilities: as discussed above, its shift to lower energy in the S_1 dark state, indicative of an increased negative charge density on the Mn_4Ca cluster compared to WT, implies that the imidazole group of D1-His332 is likely replaced by D1-Glu332 or by another nearby carboxylate group.

Comparison of D1-H332E with Other Mutants. As described in the Introduction, there are two ESEEM studies in the literature on

D1-H332 mutants from *Synechocystis* sp. PCC 6803 (D1-H332E, same as in this study) (19,21) and *Thermosynechococcus elongatus* (D1-H332S/Q) (22). Although both studies agree that D1-H332 is a ligand of Mn, there are differences in the assignment of the spin-echo signals attributed to Mn-histidine ligand N atoms; one providing support for D1-His332 and the other preferring D1-His337 which is not a direct ligand of Mn in the current crystal structures (9,10). It is suggested by the authors of ref. (22), that (i) all of the published ESEEM studies have detected D1-His337 instead of D1-His332, and (ii) the structural perturbations caused by the D1-H332E mutation eliminate the nitrogen couplings of D1-His337 (for a more detailed description see Suppl. Info.). Clarification of the source of the histidyl nitrogen coupling in PSII will require additional ESEEM studies of the S_2 state Mn_4Ca. The current XAS study on the D1-H332E mutant from *Synechocystis* sp. PCC 6803 study cannot directly resolve all the questions posed by the ESEEM studies. However, the XAS study points to the conclusion that D1-His332 directly coordinates to a Mn ion in the Mn_4Ca cluster and the altered EPR signal is a consequence of the altered OEC structure. The substantial changes seen in the structure of the Mn cluster in the mutant points to the consequences of the different ligand environment that influences the assembly, and the importance of His332 in *Synechocystis* sp. PCC 6803. The several differences of the D1-H332S and D1-H332Q mutants compared to D1-H332E, such as (1) D1-H332S and D1-H332Q evolve O_2, whereas D1-H332E does not, (2) D1-H332S and D1-H332Q exhibit a normal S_2 EPR mulitiline signal, whereas D1-H332E does not, and (3) D1-H332S and D1-H332Q shows small changes in the S_3 state, whereas D1-H332E cannot advance beyond the $S_2Y_Z^{\bullet}$ state, make the D1-H332S and D1-H332Q mutants attractive candidates for future XAS studies. Such XAS studies may also shed light on the differences between the mutants in their assembly/stability and coordination compensation/mutant rescue properties.

Concluding Remarks

On the basis of XANES and EXAFS data, we show that the D1-H332E mutation substantially alters the structure of the Mn_4Ca cluster in both the S_1 and S_2 states, resulting in an elongation of Mn-ligand and Mn-Mn interactions in the mutant. These structural perturbations are larger than those produced by any biochemical treatment or mutation examined previously with X-ray absorption spectroscopy. Because it is difficult to imagine how the D1-H332E mutation could cause these substantial structural perturbations if D1-His332 is not directly coordinated to a Mn ion, we conclude that D1-His332 ligates a Mn ion, in support of the current crystallographic structural models. In the D1-H332E mutant, Mn_4Ca cluster can be assembled but in an altered manner. This cluster advances one oxidation state (dark to illuminated state) by absorbing light, but the altered OEC structure prevents the complete catalytic cycle of the water splitting. This suggests that the first oxidation step (S_1 to S_2) takes place relatively easily, while the second step (S_2 to S_3) is critical and structurally more demanding.

References

1. McEvoy, J. P., and Brudvig, G. W. (2006) *Chem. Rev.* **106**, 4455-4483
2. McCarrick, R. M. and. Britt, R. D. (2008), Wiley-VCH Verlag GmbH & Co. KGaA, Weinheim, Germany
3. Rappaport, F., and Diner, B. A. (2008) *Coord. Chem. Rev.* **252**, 259-272
4. Renger, G., and Renger, T. (2008) *Photosynth. Res.* **98**, 53-80
5. Debus, R. J. (2008) *Coord. Chem. Rev.* **252**, 244-258
6. Yano, J., and Yachandra, V. K. (2008) *Inorg. Chem.* **47**, 1711-1726
7. Yachandra, V. K. (2005) The Catalytic Manganese-Cluster: Organization of the Metal Ions. In: Wydrzynski, T., and Satoh, S. (eds). *Photosystem II: The Light-Driven Water:Plastoquinone Oxidoreductase*, Springer, Dordrecht
8. Kamiya, N., and Shen, J. R. (2003) *Proc. Natl Acad. Sci. U. S. A.* **100**, 98-103

9. Ferreira, K. N., Iverson, T. M., Maghlaoui, K., Barber, J., and Iwata, S. (2004) *Science* **303**, 1831-1838
10. Loll, B., Kern, J., Saenger, W., Zouni, A., and Biesiadka, J. (2005) *Nature* **438**, 1040-1044
11. Guskov, A., Kern, J., Gabdulkhakov, A., Broser, M., Zouni, A., and Saenger, W. (2009) *Nat. Struct. Mol. Biol.* **16**, 334-342
12. Yano, J., Kern, J., Irrgang, K.-D., Latimer, M. J., Bergmann, U., Glatzel, P., Pushkar, Y., Biesiadka, J., Loll, B., Sauer, K., Messinger, J., Zouni, A., and Yachandra, V. K. (2005) *Proc. Natl. Acad. Sci. U. S. A.* **102**, 12047-12052
13. Grabolle, M., Haumann, M., Muller, C., Liebisch, P., and Dau, H. (2006) *J. Biol. Chem.* **281**, 4580-4588
14. Yano, J., Kern, J., Latimer, M., Sauer, K., Pushkar, Y., Messinger, J., Zouni, A., and Yachandra, V. (2007) *Photosynth. Res.* **91**, 173-173
15. Yeagle, G. J., Gilchrist, M. L., McCarrick, R. M., and Britt, R. D. (2008) *Inorg. Chem.* **47**, 1803-1814
16. Yeagle, G. J., Gilchrist, M. L., Walker, L. M., Debus, R. J., and Britt, R. D. (2008) *Philos T. R. Soc. B* **363**, 1157-1166
17. DeRose, V. J., Yachandra, V. K., McDermott, A. E., Britt, R. D., Sauer, K., and Klein, M. P. (1991) *Biochemistry* **30**, 1335-1341
18. Zimmermann, J. L., Boussac, A., and Rutherford, A. W. (1993) *Biochemistry* **32**, 4831-4841
19. Tang, X.-S., Diner, B. A., Larsen, B. S., Gilchrist, M. L., Jr., Lorigan, G. A., and Britt, R. D. (1994) *Proc. Natl. Acad. Sci. U. S. A.* **91**, 704-708
20. Debus, R. J., Campbell, K. A., Gregor, W., Li, Z. L., Burnap, R. L., and Britt, R. D. (2001) *Biochemistry* **40**, 3690-3699
21. Gilchrist, M. L. J. (1996) Pulsed Electron Paramagnetic Resonance Investigation of Photosymthetic Oxygen Evolution (Ph.D. Dissertation). In., University of California, Davis, CA
22. Sugiura, M., Rappaport, F., Hillier, W., Dorlet, P., Ohno, Y., Hayashi, H., and Boussac, A. (2009) *Biochemistry* **48**, 7856-7866
23. Debus, R. J., Campbell, K. A., Peloquin, J. M., Pham, D. P., and Britt, R. D. (2000) *Biochemistry* **39**, 470-478
24. Allahverdiyeva, Y., Deak, Z., Szilard, A., Diner, B. A., Nixon, P. J., and Vass, I. (2004) *Eur. J. Biochem.* **271**, 3523-3532
25. Strickler, M. A., Walker, L. M., Hillier, W., Britt, R. D., and Debus, R. J. (2007) *Biochemistry* **46**, 3151-3160
26. Boussac, A., Rappaport, F., Carrier, P., Verbavatz, J. M., Gobin, R., Kirilovsky, D., Rutherford, A. W., and Sugiura, M. (2004) *J. Biol. Chem.* **279**, 22809-22819
27. Strickler, M. A., Walker, L. M., Hillier, W., and Debus, R. J. (2005) *Biochemistry* **44**(24), 8571-8577
28. Chu, H.-A., Nguyen, A. P., and Debus, R. J. (1994) *Biochemistry* **33**, 6137-6149
29. George, G. N., Pickering, I. (2000) EXAFSPAK and EDG_FIT. In., Stanford Synchrotron Radiation Lightsource, Stanford Linear Accelerator Center, Stanford University, Stanford, CA
30. Newville, M. (2001) *J. Synchrotron Radiat.* **8**, 322-324
31. Rehr, J. J., and Albers, R. C. (2000) *Rev. Mod. Phys.* **72**, 621-654
32. Messinger, J., Robblee, J. H., Bergmann, U., Fernandez, C., Glatzel, P., Visser, H., Cinco, R. M., McFarlane, K. L., Bellacchio, E., Pizarro, S. A., Cramer, S. P., Sauer, K., Klein, M. P., and Yachandra, V. K. (2001) *J. Am. Chem. Soc.* **123**, 7804-7820
33. Liang, M. C., Latimer, M. J., Dau, H., Roelofs, T. A., Yachandra, V. K., Sauer, K., and Klein, M. P. (1994) *Biochemistry* **33**, 4923-4932
34. Chu, H.-A., Nguyen, A. P., and Debus, R. J. (1995) *Biochemistry* **34**, 5859-5882
35. Ghanotakis, D. F., Babcock, G. T., and Yocum, C. F. (1984) *FEBS Letters* **167**, 127-130
36. Cinco, R. M., Robblee, J. H., Rompel, A., Fernandez, C., Yachandra, V. K., Sauer, K., and Klein, M. P. (1998) *J. Phys. Chem. B* **102**, 8248-8256
37. Pushkar, Y. L., Yano, J., Sauer, K., Boussac, A., and Yachandra, V. K. (2008) *Proc. Natl. Acad. Sci. U. S. A.* **105**, 1879-1884

38. Yano, J., Kern, J., Sauer, K., Latimer, M., Pushkar, Y., Biesiadka, J., Loll, B., Saenger, W., Messinger, J., Zouni, A., and Yachandra, V. K. (2006) *Science* **314**, 821-825
39. Yano, J., Pushkar, Y., Glatzel, P., Lewis, A., Sauer, K., Messinger, J., Bergmann, U., and Yachandra, V. K. (2005) *J. Am. Chem. Soc.* **127**, 14974-14975
40. DeRose, V. J., Mukerji, I., Latimer, M. J., Yachandra, V. K., Sauer, K., and Klein, M. P. (1994) *J. Am. Chem. Soc.* **116**, 5239-5249
41. Cinco, R. M., Rompel, A., Visser, H., Aromi, G., Christou, G., Sauer, K., Klein, M. P., and Yachandra, V. K. (1999) *Inorg. Chem.* **38**, 5988-5998
42. Cinco, R. M., Holman, K. L. M., Robblee, J. H., Yano, J., Pizarro, S. A., Bellacchio, E., Sauer, K., and Yachandra, V. K. (2002) *Biochemistry* **41**, 12928-12933
43. Cinco, R. M., Robblee, J. H., Messinger, J., Fernandez, C., Holman, K. L. M., Sauer, K., and Yachandra, V. K. (2004) *Biochemistry* **43**, 13271-13282
44. Latimer, M. J., DeRose, V. J., Yachandra, V. K., Sauer, K., and Klein, M. P. (1998) *J. Phys. Chem. B* **102**, 8257-8265
45. Latimer, M. J., DeRose, V. J., Mukerji, I., Yachandra, V. K., Sauer, K., and Klein, M. P. (1995) *Biochemistry* **34**, 10898-10909
46. Dau, H., Andrews, J. C., Roelofs, T. A., Latimer, M. J., Liang, W. C., Yachandra, V. K., Sauer, K., and Klein, M. P. (1995) *Biochemistry* **34**, 5274-5287
47. Baldwin, M. J., Stemmler, T. L., Riggs-Gelasco, P. J., Kirk, M. L., Penner-Hahn, J. E., and Pecoraro, V. L. (1994) *J. Am. Chem. Soc.* **116**, 11349-11356
48. Mukhopadhyay, S., Mandal, S. K., Bhaduri, S., and Armstrong, W. H. (2004) *Chem. Rev.* **104**, 3981-4026
49. Pushkar, Y., Yano, J., Glatzel, P., Messinger, J., Lewis, A., Sauer, K., Bergmann, U., and Yachandra, V. (2007) *J. Biol. Chem.* **282**, 7198-7208
50. Britt, R. D., Zimmermann, J.-L., Sauer, K., and Klein, M. P. (1989) *J. Am. Chem. Soc.* **111**, 3522-3532
51. Burnap, R. L. (2004) *Phys. Chem. Chem. Phys.* **6**, 4803-4809
52. Dasgupta, J., Ananyev, G. M., and Dismukes, G. C. (2008) *Coord. Chem. Rev.* **252**, 347-360
53. Dau, H., Liebisch, P., and Haumann, M. (2005) *Phys. Scripta* **T115**, 844-846

Footnotes

*This work was supported by the NIH (GM 55302 to V. K. Y and GM 076232 to R. J. D.), and by the DOE, Director, Office of Science, Office of Basic Energy Sciences (OBES), Division of Chemical Sciences, Geosciences, and Biosciences, under Contract DE-AC02-05CH11231 (to J. Y. and V. K. Y.). Portions of this research were carried out at SSRL, operated by Stanford University for DOE, OBES. The SSRL Structural Molecular Biology Program is supported by the DOE, Office of Biological and Environmental Research and by the NIH, NCRR. We thank Dr. Yulia Pushkar, Xi Long, and Thomas Lohmiller for help with XAS data collection, and Profs. R. David Britt, Ken Sauer and Dr. Jan Kern for useful discussions.

The abbreviations used are: PSII, photosystem II; OEC, oxygen-evolving complex; WT, wild type; XAS, X-ray absorption spectroscopy; XANES, X-ray absorption near edge structure, EXAFS; extended X-ray absorption fine structure, EPR; electron paramagnetic resonance, ESEEM; electron spin echo envelope Modulation.

Figure Legends

Fig. 1. Ligand environment of the OEC obtained from X-ray crystallography (a,b),(9,10) and putative ligand environment from the single crystal EXAFS study (c)(38). In (c), Model II and III from the ref.(38) are shown.

Fig. 2. Mn XANES and 2nd derivative spectra of (a) Synechocystis WT S_1 (black) and S_2 (gray) states, (b) a comparison of Synechocystis WT (black) and D1-H332E mutant (gray) S_1 state spectra, and (c) D1-H332E mutant dark (gray) and illuminated (black) samples. The bottom part shows the 2nd derivative spectra of XANES, and zero-crossing energy gives the rising edge inflection point, which is indicated.

Fig. 3. Fourier transforms of the Mn EXAFS spectra of (a) Synechocystis WT S_1 (black) and S_2(gray) states and (b) D1-H332E mutant dark (black) and illuminated (gray) states.

Fig. 4. Fourier transforms of the Sr XANES and EXAFS spectra of Synechocystis D1-H332E mutant dark state (gray). For comparison, Sr XANES and EXAFS spectra of *Synechococcus elongatu*s WT S_1 state (black) are shown (37).

Fig. 5. Mn EXAFS curve fitting result of (a) Synechocystis WT S_1 state and (b) D1-H332E dark state. Black is the experimental data. Fit# 2 and 4 in Table 1 for the WT and Fit# 2 and 8 for the D1-H332E in Table 2 are shown in the figure.

Fig. 6. Sr EXAFS curve fitting result of Synechocystis D1-H332E S_1 state. Black is the experimental data. Fit# 1 and 2 in Table 3 are shown in the figure.

Fig. 7. Possible structural reasons for the Mn•••Mn elongation in the mutant: (a) protonation of the bridging oxygen and (b) bidentate to monodentate change.

Table 1. EXAFS curve fitting parameters for the WT S_1 state.

Table 2. EXAFS curve fitting parameters for Synechocystis D1-H332E mutant dark state.

Table 3. EXAFS curve fitting parameters for the Sr-substituted D1-H332E mutant dark state.

Table 1: Curve Fitting Results of Synechocystis WT S_1 state EXAFS spectrum.

Fit No.	Mn-O			Mn-Mn			Mn-Mn			Mn-Ca			Mn-C			R_f
	R (Å)	N[a]	σ^2 (Å^2)	R (Å)	N[b]	σ^2 (Å^2)	R (Å)	N	σ^2 (Å^2)	R (Å)	N	σ^2 (Å^2)	R (Å)	N[c]	σ^2 (Å^2)	(%)
1	1.87	**6.0**	0.011	2.72	**1.5**	0.004	3.24	**0.5**	0.003	**3.41**	**0.5**	**0.005**				23.3
2	1.87	**6.0**	0.012	2.72	**1.5**	0.004	3.23	**0.5**	0.003	**3.41**	**0.75**	**0.005**				23.7
3	1.87	**6.0**	0.012	2.72	**1.5**	0.004	3.25	**0.5**	0.004	**3.41**	**0.5**	**0.005**	3.20	**2.75**	0.018	19.5
4	1.86	**6.0**	0.012	2.72	**1.5**	0.004	3.24	**0.5**	0.003	**3.41**	**0.75**	**0.005**	3.20	**2.75**	0.018	20.1

* k-range of 2.5-11.4 Å^{-1} was used for the fitting.
* Bold letters indicate fixed parameters.
* E_0=6561.3 eV, S_0^2=0.85.

[a] The MnO (~1.8 Å) coordination number was fixed to N=6.0 for simplicity, assuming hexa-coordination for all four Mn. Note that if one Mn out of four is penta-coordinate as suggested by the literature (53), the N value becomes 5.75. However, this does not cause a noticeable effect on the fit quality.

[b] N values are defined as the total number of absorber-backscatterer vectors divided by the number of absorber atoms per OEC. For example, N=1.5 implies that there are three Mn-Mn ~ 2.7 Å interactions.

[c] The MnC (~3.2 Å) coordination number was fixed to N=2.75, based on the ligand model of the 2.9 Å crystal structure (11). Approximately, each Mn sees two to four carbons of carboxylate groups and an imidazole ring, although these numbers remain somewhat ambiguous at the 2.9 Å structure due to its moderate resolution. However, the contribution of this path to the fitting quality is minor due to the high Debye-Waller factor.

Table 2: Curve Fitting Results of His332Glu dark state EXAFS spectrum.

Model	Fit No.	Mn-O			Mn-Mn			Mn-Mn			Mn-Ca			R_f
		R (Å)	N [b]	σ^2 (Å^2)	R (Å)	N	σ^2 (Å^2)	R (Å)	N	σ^2 (Å^2)	R (Å)	N	σ^2 (Å^2)	(%)
3:1:x [a]	1	1.89	**6.0**	0.009	2.77	**1.5**	0.006	3.21	**0.5**	0.002	**3.41**	**0.5**	0.004	9.6
	2	1.89	**6.0**	0.009	2.77	**1.5**	0.006	3.21	**0.5**	0.003	**3.41**	**0.75**	0.007	9.6
3:2:x	3	1.89	**6.0**	0.009	2.77	**1.5**	0.007	3.22	**1.0**	0.008	**3.41**	**0.5**	0.007	9.6
	4	1.89	**6.0**	0.009	2.77	**1.5**	0.007	3.21	**1.0**	0.009	**3.41**	**0.75**	0.010	9.6
2:2:x	5	1.89	**6.0**	0.009	2.76	**1.0**	0.004	3.20	**1.0**	0.005	**3.41**	**0.5**	0.002	9.6
	6	1.89	**6.0**	0.009	2.76	**1.0**	0.004	3.20	**1.0**	0.005	**3.41**	**0.75**	0.005	9.6
2:1:x	7	1.89	**6.0**	0.009	2.76	**1.0**	0.004	3.22	**0.5**	**0.003**	**3.41**	**0.5**	0.007	9.8
	8	1.89	**6.0**	0.009	2.77	**1.0**	0.004	3.22	**0.5**	**0.003**	**3.41**	**0.75**	0.009	9.7

* k-range of 2.5-11.4 Å^{-1} was used for the fitting.
* Bold letters indicate fixed parameters.
* E_0=6561.3 eV, S_0^2=0.85.

[a] This indicates the number of interactions in the model, di-μ-oxo bridged Mn-Mn(2.7 Å) : mono-μ-oxo bridged Mn-Mn(3.3 Å) : Mn-Ca(3.4 Å). The MnCa fragment (x) was changed either to x=2 (N=0.5) or x=3 (N=0.75) based on our previous study using Sr-substituted PSII (37).

[b] Hexa-coordination for all four Mn was assumed for simplicity.

Table 3: Curve Fitting Results of Sr-substituted His332Glu dark state Sr EXAFS spectrum.

Fit No.	Sr-O			Sr-Mn			Sr-Mn			R_f
	R (Å)	N[a]	σ^2 (Å^2)	R (Å)	N	σ^2 (Å^2)	R (Å)	N	σ^2 (Å^2)	(%)
1	2.56	**8**	0.005	3.50	**3**	0.009	3.94	**1**	0.012	9.8
2	2.55	**8**	0.005	3.48	**2**	0.006	3.92	**2**	0.009	12.1
3	2.55	**8**	0.005	3.47	**2**	0.006	3.84	**1**	0.012	14.4

* k-range of 2.7-12.8 Å^{-1} was used for the fitting.
* Bold letters indicate fixed parameters.
* E_0=16120.0 eV, S_0^2=0.99.
[a] The coordination number N was fixed to 8.

Figure 1

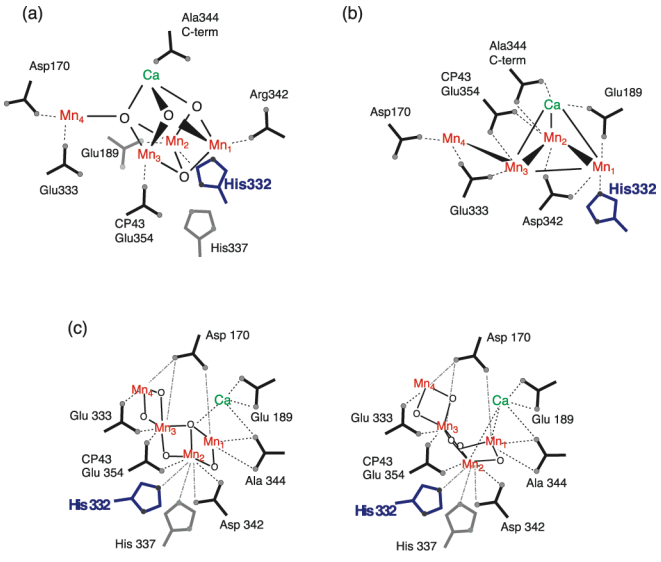
(a)
Ala344
C-term
Asp170
Ca
Arg342
Mn4
O
O
O
Mn2
Mn1
Glu189
Mn3
O
His332
Glu333
CP43
Glu354
His337
(b)
Ala344
C-term
CP43
Glu354
Glu189
Ca
Asp170
Mn4
Mn2
Mn3
Mn1
His332
Glu333
Asp342
(c)
Asp 170
Mn4
Ca
Glu 333
Glu 189
Mn3
Mn1
CP43
Glu 354
Mn2
Ala 344
His 332
Asp 342
His 337
Asp 170
Mn4
Ca
Glu 333
Glu 189
Mn3
Mn1
CP43
Glu 354
Mn2
Ala 344
His 332
Asp 342
His 337

Figure 2

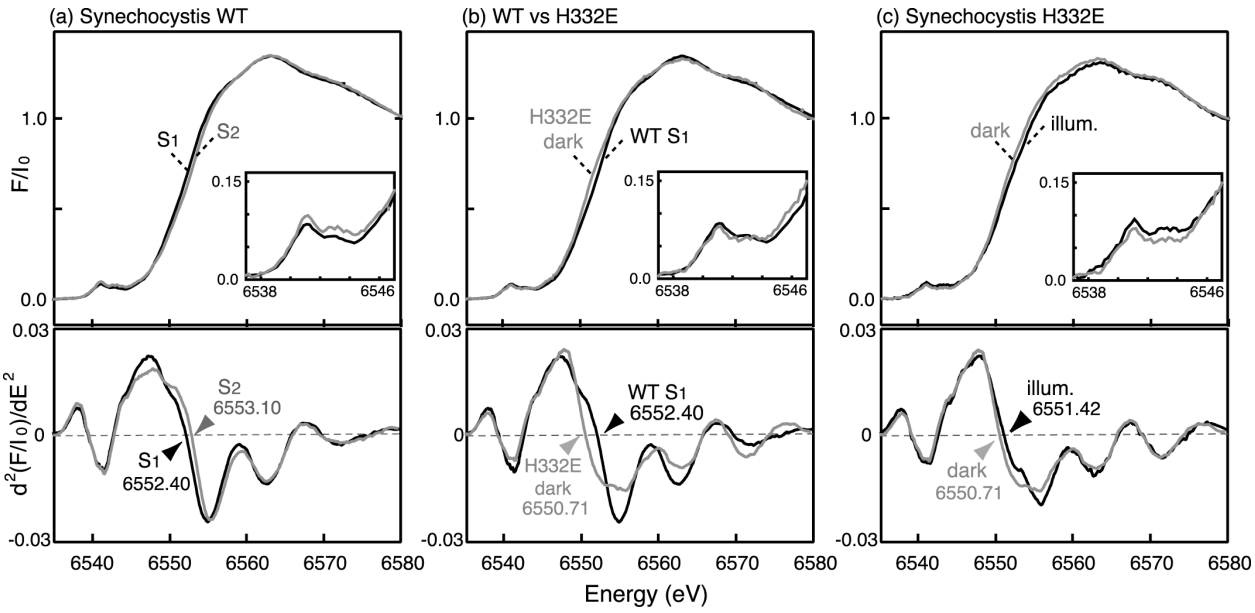
(a) Synechocystis WT
(b) WT vs H332E
(c) Synechocystis H332E
F/I0
S1
S2
H332E
dark
WT S1
dark
illum.
0.15
0.0
6538
6546
1.0
0.0
0.03
-0.03
d2(F/I0)/dE2
S2
6553.10
S1
6552.40
WT S1
6552.40
H332E
dark
6550.71
illum.
6551.42
dark
6550.71
6540
6550
6560
6570
6580
Energy (eV)

Figure 3

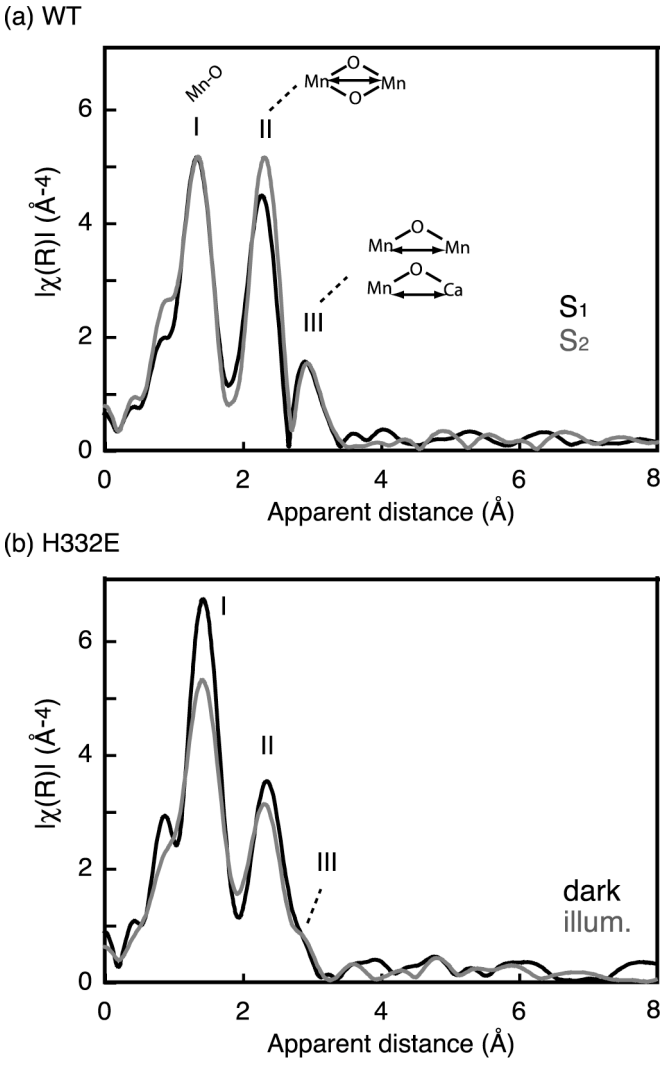
(a) WT
Mn-O
I
II
III
Mn
O
Mn
O
Mn
O
Mn
Mn
O
Mn
Ca
S1
S2
|χ(R)| (Å-4)
Apparent distance (Å)
(b) H332E
I
II
III
dark
illum.
|χ(R)| (Å-4)
Apparent distance (Å)

Figure 4

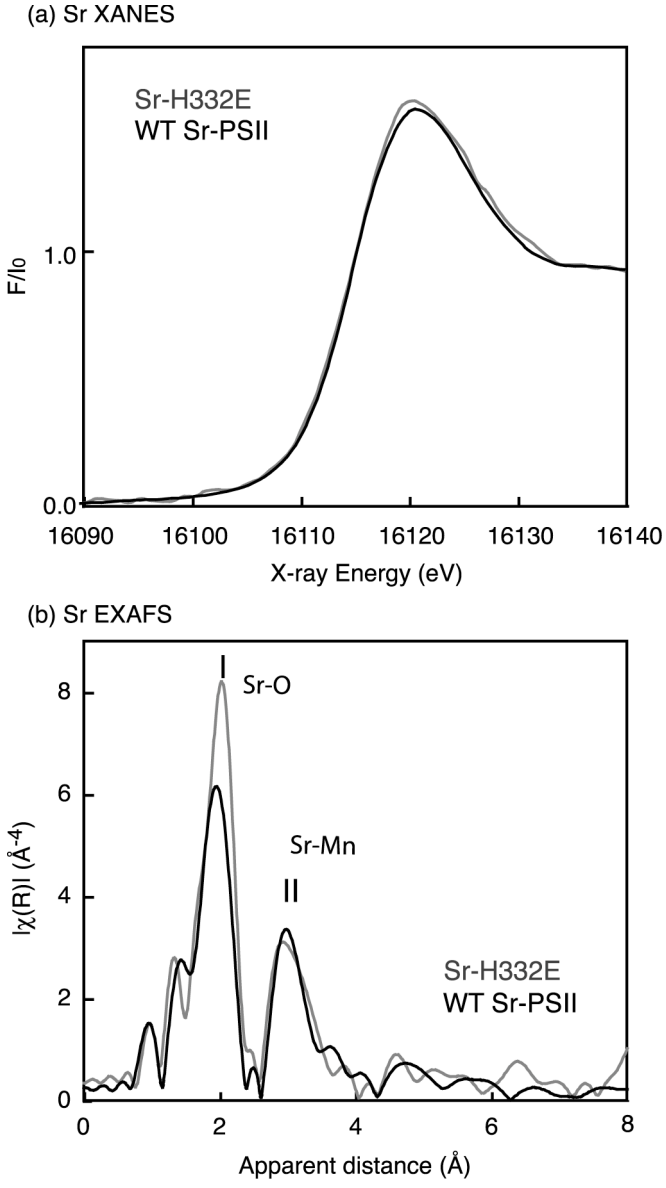
(a) Sr XANES
Sr-H332E
WT Sr-PSII
F/Io
1.0
0.0
16090
16100
16110
16120
16130
16140
X-ray Energy (eV)
(b) Sr EXAFS
I
Sr-O
Sr-Mn
II
Sr-H332E
WT Sr-PSII
|χ(R)| (Å-4)
8
6
4
2
0
0
2
4
6
8
Apparent distance (Å)

Figure 5

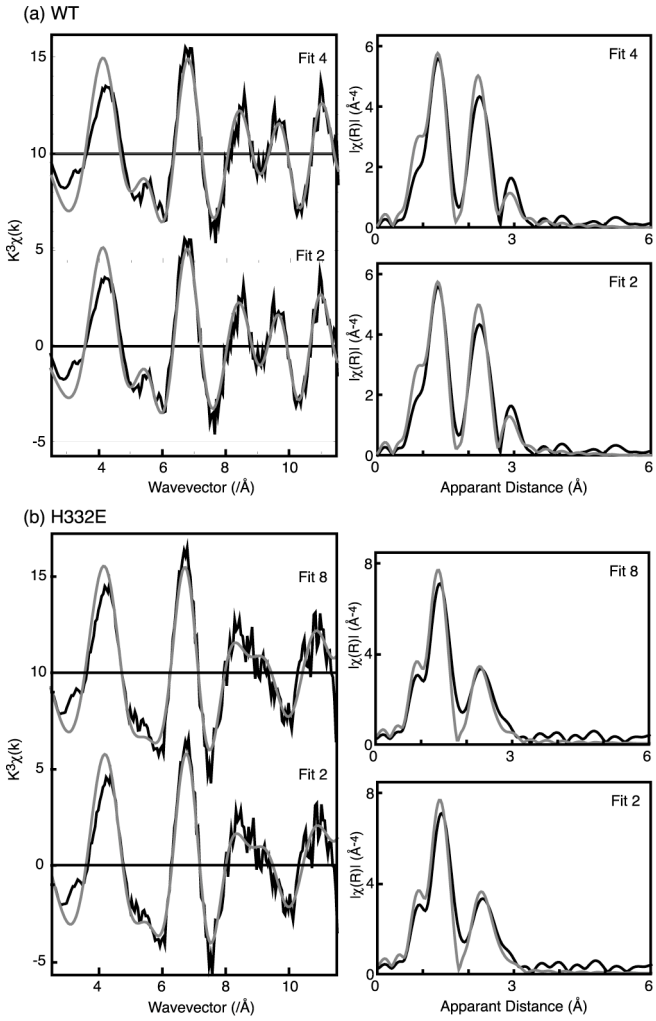
(a) WT
Fit 4
Fit 2
$k^3\chi(k)$
Wavevector (/Å)
$|\chi(R)|$ (Å^{-4})
Apparant Distance (Å)
(b) H332E
Fit 8
Fit 2
$k^3\chi(k)$
Wavevector (/Å)
$|\chi(R)|$ (Å^{-4})
Apparant Distance (Å)

Figure 6

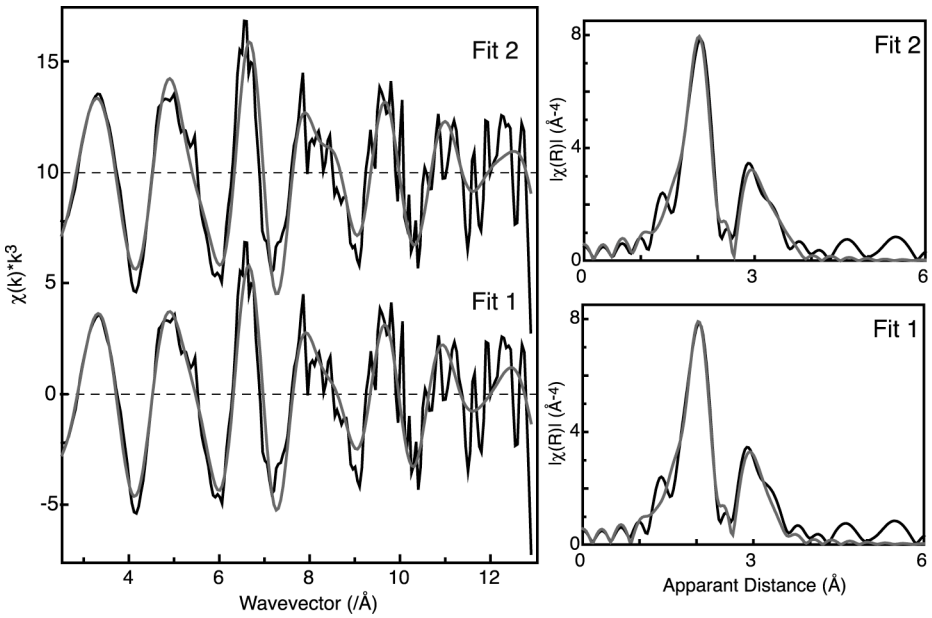

Figure 7

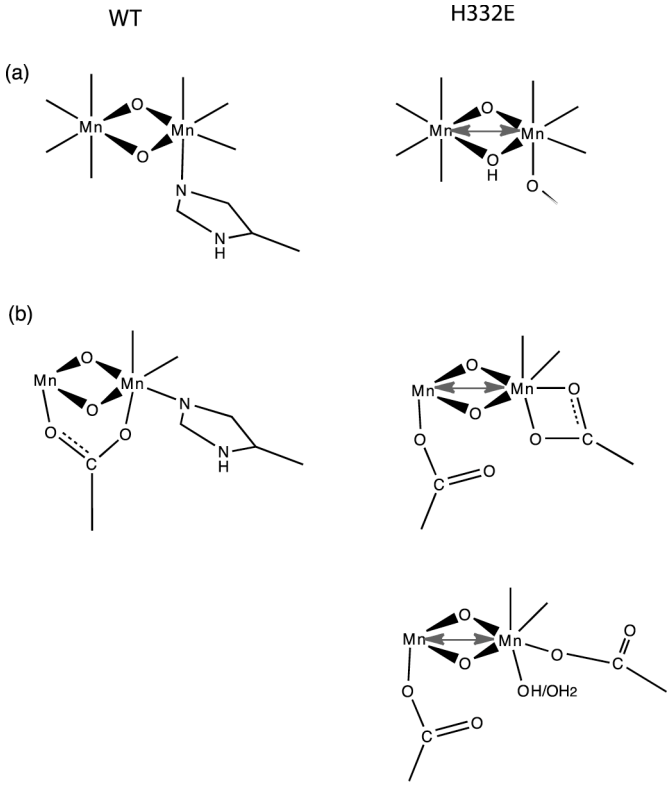

DISCLAIMER